Inorganic Chemistry

Article

pubs.acs.org/IC

Structural Distortion of Molybdenum-Doped Manganese Oxide Octahedral Molecular Sieves for Enhanced Catalytic Performance

Chun-Hu Chen,[†,‡] Eric C. Njagi,[†] Sheng-Yu Chen,[†] Dayton T. Horvath,[†] Linping Xu,[†] Aimee Morey,[†,§] Charles Mackin,[†] Raymond Joesten,[†] and Steven L. Suib*[,†]

[†]Department of Chemistry, University of Connecticut, Storrs, Connecticut 06269, United States

[‡]Department of Chemistry, National Sun Yat-sen University, Kaohsiung, Taiwan 80424, United States

[§]Department of Chemistry, United States Air Force Academy, Colorado Springs, Colorado 80840, United States

Supporting Information

ABSTRACT: Due to the excellent catalytic performance of manganese oxide (K-OMS-2) in a wide range of applications, incorporation of various dopants has been commonly applied for K-OMS-2 to acquire additional functionality or activities. However, the understanding of its substitution mechanism with respect to the catalytic performance of doped K-OMS-2 materials remains unclear. Here we present the structural distortion (from tetragonal to monoclinic cell) and morphological evolution in K-OMS-2 materials by doping hexavalent molybdenum. With a Mo-to-Mn ratio of 1:20 (**R-1:20**) in the preparation, the resultant monoclinic K-OMS-2 shows a small equidimensional particle size (~15 nm), a high surface area of 213 m^2g^{-1}, and greatly improved catalytic activity toward CO oxidation with lower onset temperatures (40 °C) than that of pristine K-OMS-2 (above 130 °C). HR-TEM analyses reveal direct evidence of structural distortion on the cross-section of 2 × 2 tunnels with the absence of 4-fold rotation symmetry expected for a tetragonal cell, which are indexed using a monoclinic cell. Our results suggest that substitution of Mo^{6+} for Mn^{3+} (rather than Mn^{4+}) coupled with the vacancy generation results in a distorted structure and unique morphology. The weakened Mn−O bonds and Mn vacancies associated with the structural distortion may be mainly responsible for the enhanced catalytic activity of monoclinic K-OMS-2 instead of dopant species.

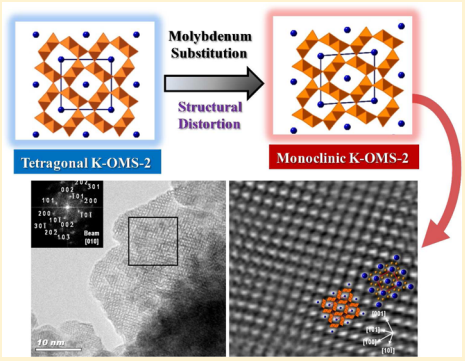

1. INTRODUCTION

Manganese oxides with cryptomelane-type structure (also known as octahedral molecular sieve, K-OMS-2, or α-MnO_2),[1,2] possessing unique porosity, tunnel structures, mixed valency, and semiconductivity, have shown promising performance in clean energy, batteries, heterogeneous catalysis, and environmental protection.[3−11] The versatility of K-OMS-2 is mainly attributed to its unique and complex structures composed of double-wide slabs of edge-shared MnO_6 octahedra, joined together through corner-shared oxygens to produce a structure characterized by 2 × 2 octahedra-wide tunnels (Figure 1).[1,12] Typical K-OMS-2, with the tetragonal cell shown in Figure 1a and 1b, exhibits one-dimensional fibrous morphology elongated parallel to the tunnel axis. The mixed valency in K-OMS-2 contributes to its highly active and selective catalysis, due the reduction of six-coordinated Mn^{4+} to Mn^{3+} compensated by the presence of K^+ ions in tunnel sites.[13,14]

To further extend the functionality of K-OMS-2 (e.g., magnetic or photoactive K-OMS-2), structural incorporation of various dopants has been an effective strategy.[15,16] Dopants like Ag^+, Mg^{2+}, Ni^{2+}, Cu^{2+}, Cr^{3+}, In^{3+}, Ce^{4+}, V^{5+}, Fe^{3+}, Co^{2+}, and W^{6+} have been incorporated into K-OMS-2 materials for various applications.[10,16−23] However, due to the structural complexity, these works show no comprehensive understanding regarding the substitution mechanism of K-OMS-2 or how such substitution influences the material performance. The major challenge comes from the problematic structural characterization, concomitant with the inability to produce systematic evolution of material properties for systematic studies. Recent advances suggest that structural distortion may be linked to the extraordinary activity of doped K-OMS-2,[24] but similar difficulties of structural analyses again hinder finding key evidence for the precise control of catalytic efficiency.

In this work, we report the significant changes of morphology, particle sizes, catalytic activities, and structural distortions of Mo^{6+}-substituted K-OMS-2 materials. Selection of hexavalent molybdenum is aimed at eliminating the possibility of tunnel cation substitution, forcing replacement of manganese cations in the octahedral framework and producing ideal probes to study correlations between structural substitution and catalytic activities. We observed direct evidence of tunnel cross-section images with a "distorted" symmetry (from the higher structural symmetry of tetragonal to monoclinic systems, Figure 1c) after Mo^{6+} doping. A

Received: April 23, 2015
Published: October 9, 2015

DOI: 10.1021/acs.inorgchem.5b00906
Inorg. Chem. 2015, 54, 10163−10171

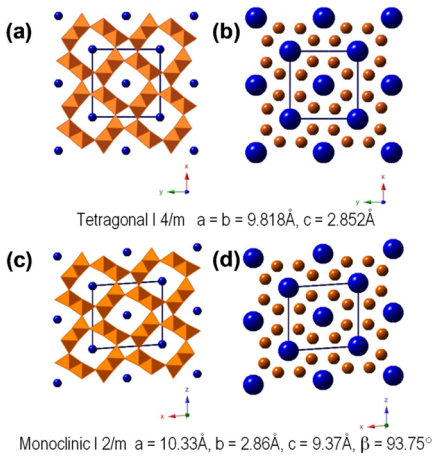

Figure 1. Structures of tetragonal (a and b) and monoclinic (c and d) cryptomelane-type manganese oxide (K-OMS-2). Manganese is illustrated as MnO_6 octahedra (a and c) and as small spheres (b and d) in orange. Potassium ions (blue spheres) appear at corners and the center of the unit cell in a projection along [001] in the tetragonal polymorph and along [010] in the monoclinic polymorph. Lattice parameters are from this work. Drawn using CrystalMaker.

substitution pathway of Mo^{6+} for Mn^{3+} is proposed based on compositional analyses. Our results also indicate a strong enhancement in CO oxidation catalysis mainly due to the structural distortion of the monoclinic structures.

2. EXPERIMENTAL SECTION

2.1. Synthesis. All materials were prepared using the single-step reflux method.[21,25] To prepare undoped K-OMS-2, a solution with 5 g (0.032 mol) of $KMnO_4$ in 100 mL of distilled deionized water (DDW) was prepared (solution A). Solution B was then prepared by dissolving 7.5 g (0.044 mol) of $MnSO_4{\cdot}H_2O$ in 50 mL of DDW and adding 8.5 mL of nitric acid. Solution B was subsequently added dropwise into solution A with vigorous stirring forming a dark precipitate through redox reaction between Mn^{2+} and Mn^{7+}. The resultant slurry was refluxed overnight at 100 °C, washed, and dried at 120 °C for 12 h to obtain K-OMS-2. Mo-doped material, denoted as [Mo] K-OMS-2, was prepared by adding Na_2MoO_4 to solution A. [Mo] K-OMS-2 materials were prepared with Mo/Mn molar ratios of 1/100, 1/50, 1/20, and 1/10 in the starting mixture. These samples are denoted as **R-1:100**, **R-1:50**, **R-1:20**, and **R-1:10**, respectively. The controlled sample of nonsubstituted K-OMS-2 is denoted as **Blank K-OMS-2**. Following the suggestion of a reviewer, we synthesized an additional sample with molar Mo/Mn in the ratio 1/30, denoted as **R-1:30**, to better characterize the transition between low Mo prismatic tetragonal [Mo] K-OMS-2 and high Mo flake-like monoclinic [Mo] K-OMS-2. Characterization of this sample was limited to XRD and bright field TEM.

2.2. Material Characterization. The powder X-ray diffraction (XRD) patterns were obtained using a Scintag 2000 XDS-2000 diffractometer with Cu Kα (λ = 0.15406 nm) radiation. The beam voltages and currents were 45 kV and 40 mA, respectively. Microstructures and morphologies of the synthesized materials were studied using transmission electron microscopy (TEM). Low-resolution, bright field TEM images were obtained using a FEI Tecnai T12 TEM/STEM microscope equipped with an energy-dispersive (EDXS) detector at an accelerating voltage of 120 kV. High-resolution TEM micrographs were recorded using a JEOL 2010 FasTEM microscope operating at an accelerating voltage of 200 kV. The surface areas of the synthesized materials were determined by the Brunauer–Emmett–Teller (BET) method using a Micrometrics ASAP 2010 instrument. Nitrogen physisorption experiments were carried out at 77 K after initial pretreatment of the samples by degassing at 150 °C for 2 h. Fourier transform infrared (FTIR) spectra were acquired using a Nicolet Magna-IR System 750 spectrometer with a MCT-B detector. The samples were diluted with KBr and then pressed into pellets. Raman spectroscopy was performed at 514 nm with a Renishaw Ramanscope. Spectra of the as-prepared samples were collected at 64 scans with a scan rate of 126 per minute. Analyses were done at a minimum of 5 spots for each sample to verify the reproducibility of the collected spectra. The thermal stability of the synthesized materials was determined using a Hi-Res TGA 2950 Thermogravimetric Analyzer in an N_2 atmosphere. The average oxidation state of manganese in the as-synthesized materials was measured experimentally (AOS_{meas}) using a potentiometric titration method as described in the literature.[26] The total manganese content was determined by digesting the samples using concentrated HCl to convert all of the manganese to Mn^{2+} and titrating to Mn^{3+} using standardized $KMnO_4$. The AOS of manganese was then determined by reducing the manganese to Mn^{2+} with $(NH_3)_2Fe(SO_4)_2$ and back-titrating the excess Fe^{2+} with the $KMnO_4$ standard solution.

The elemental composition, particularly for K, Mn, and Mo, was determined by combining the data of atomic absorption (AA), XPS, and energy-dispersive X-ray spectroscopy (EDXS). Mole percents of K and Mn were determined by AA, while the ratios of Mo/Mn were determined by XPS due to signal interference between Mn and Mo in AA. We used semiquantitative elemental analyses of EDXS to confirm that the AA and XPS analyses are representative of individual grains. The concentrations of manganese and potassium in the samples were determined using a PerkinElmer model 3100 Flame Atomic Absorption Spectrometer (FAAS). Standard calibration curves were created using atomic absorption standard solutions (Sigma-Aldrich) diluted to the desired concentrations. The samples were digested using a mixture of HCl and H_2O_2 with a volume ratio of 1:10. For XPS experiments, the oxidation states and atomic surface concentrations of Mo were determined using a Leybold-Heraeus model 3000 spectrometer equipped with a SPECS EA10MCD energy analyzer. The signal from adventitious carbon (binding energy of 284.6 eV) was used as a reference for binding energies.

2.3. CO Oxidation Catalytic Test. The CO oxidation tests were conducted in a quartz tubular fixed bed flow reactor at atmospheric pressure with 100 mg of catalysts. The catalysts were purged by flowing He for 2 h at 180 °C before analyses to remove adsorbed species. The composition of feed gas was 1% CO, 2% O_2, and 5% N_2 in helium. The space velocity in all experiments was 35 000 mL h^{-1} g_{cat}^{-1}. Nitrogen was used as an internal standard for gas chromatography (GC). An online gas chromatograph (SRI 8610C GC) equipped with a silica gel column and a TCD detector were used to analyze the reaction products. Catalytic data were collected after 30 min stabilization at each analysis temperature.

3. RESULTS

3.1. Structural Characterization. The XRD patterns of four [Mo] K-OMS-2 materials and **Blank K-OMS-2** are shown in Figure 2, and lattice parameters and critical d spacings are listed in Table S-1. The broad hump centered at about 22° 2θ in all samples was attributed to the glass sample holder. All peaks are accounted for as tetragonal K-OMS-2, but there are tiny shifts in peak position related to Mo concentrations (Table S-1). Lattice parameters and d spacings measured for the **Blank K-OMS-2** are a close match for those of a Rietveld-refined sample reported by Gao et al.[14] The patterns for Mo-doped **R-1:100**, **R-1:50**, and **R-1:30** are very similar to that of **Blank K-OMS-2** but show a shift of peaks to higher 2θ corresponding to smaller d spacings. The differences of d_{110}, the translation perpendicular to the tunnel walls, are −0.043, −0.014, and 0.000 Å for **R-1:100**, **R-1:50**, and **R-1:30** and −0.012, −0.006, and −0.008 Å for d_{001}, the translation along the tunnel axis.

The XRD patterns of **R-1:20** show significant peak broadening with little difference in intensity compared with the other samples, and peaks are shifted to smaller 2θ relative to

DOI: 10.1021/acs.inorgchem.5b00906
Inorg. Chem. 2015, 54, 10163−10171

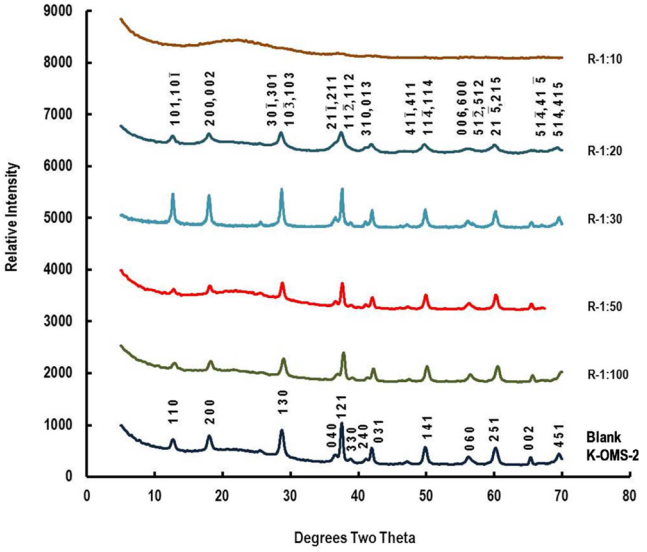

Figure 2. X-ray diffraction patterns of the K-OMS-2 blank and [Mo] K-OMS-2 materials. Peaks for the blank (**Blank OMS-2**), **R-1:100**, and **R-1:50** are indexed for the tetragonal structure; peaks for **R-1:20** indexed for the monoclinic structure, although *h0l* doublets and quartets are not resolved.

the blank. No impurity phases corresponding to molybdenum oxides or others were observed. Crystallite sizes of 10 nm were determined with the Scherrer equation. **R-1:10** shows no diffraction peak, suggesting an extreme peak broadening effect and/or structural collapse (amorphous feature) due to high content of Mo substitution. The similar tendency of peak broadening was reported in high-valent species of V^{5+}- and W^{6+}-incorporated K-OMS-2[21,23] but not for dopants with lower valence such as In(III), (Fe(III), and Co(II).[22,27,28] The strong dependence of valence numbers of dopants on the stability of K-OMS-2 phase implies the critical role of charge compensation of principle concern in the substitution mechanism.

Morphology studies show systematic changes in grain size and shape with increasing contents of Mo (Figure 3). In general, the Mo-doped samples show a decrease of aspect ratios (defined as length/width) with increasing concentrations of molybdenum (Table 1). One-dimensional (or rod-like) crystals occur in the **Blank K-OMS-2** and **R-1:100**, elongated parallel

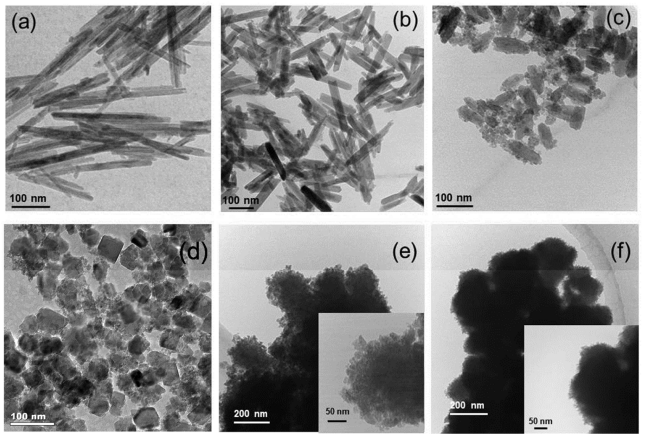

Figure 3. Bright field TEM images of K-OMS-2 and [Mo] K-OMS-2 materials: (a) **Blank K-OMS-2**, (b) **R-1:100**, (c) **R-1:50**, (d) **R-1:30**, (e) **R-1:20**, and (f) **R-1:10**.

Table 1. Particle Diameter, Average Aspect Ratio, and BET Surface Area of Pristine and Mo-Doped K-OMS-2 Materials

sample	particle diameter (nm)	average aspect ratio	S_{BET} (m^2/g)
Blank K-OMS-2	13.7 ± 1.4	15.2	86
R-1:100	25.5 ± 4.7	6.1	53
R-1:50	35.9 ± 4.7 and 9.1 ± 1.9[a]	2.5 and 1.1[a]	76
R-1:20	6.5 ± 2.1	1.1	213
R-1:10	NA[b]	NA[b]	347

[a]Two different particle morphologies in this sample. [b]No precise particle dimension available due to flake-like morphology.

to the tunnel axis of [001] (Figure S-1). **R-1:50** and **R-1:30** clearly show a mixture of two morphologies of particles, the large-volume blade and cubic-like grains (corresponding to **R-1:50** and **R-1:30**, respectively) with fine nanoflakes. **R-1:20** and **R-1:10** demonstrate a single morphology of ultrafine nanoflakes, similar to these in **R-1:50** and **R-1:30** but quite different from the samples with relatively low Mo content. The measured diameters of flake-shaped grains in **R-1:20** are 6.5 ± 2 nm and smaller than these for **R-1:10**. The systematic changes of morphology consistent with the incorporation of Mo suggest the successful incorporation of Mo dopant in the structure of K-OMS-2 rather than the local segregation of molybdenum oxide species. With the presence of different nanocrystals in **R-1:50** and **R-1:30** (Figure 3c and 3d), both these samples represent the critical state that bridges the transformation from bladed crystals to ultrafine flakes. In addition, **R-1:20** is the only sample that possesses the K-OMS-2 structure and also shows ultrafine flaked shape. Detailed structural analyses of these samples can be informative in revealing the shape-evolution mechanism.

3.2. Structural Distortion. We further acquired the high-resolution (HR) TEM images of **R-1:100**, **R-1:50**, and **R-1:20** to investigate the possible mechanism of shape evolution. **R-1:100** shows the (110) fringes parallel to the long axis of the 1D fibers (Figure S-1), similar to the undoped K-OMS-2.[14] Figure 4a shows the part of a blade-shaped crystal of **R-1:50** in

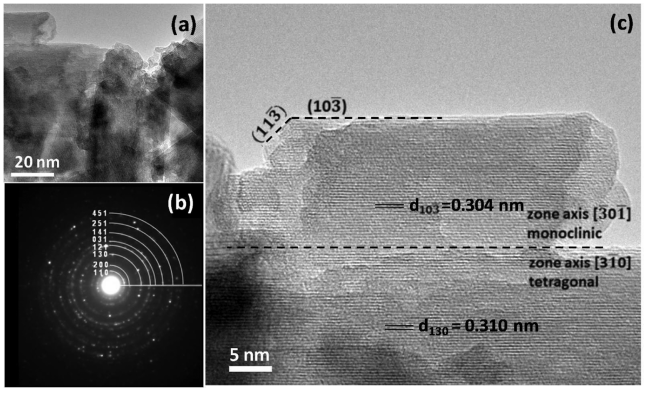

Figure 4. HRTEM images and polycrystalline SAED of **R-1:50**. (a) Image of a large crystal partially overlain and surrounded by smaller equidimensional crystals. (b) SAED patterns of this area correspond to K-OMS-2 and are indexed based on the tetragonal cell. (c) Enlargement of the top-left area in a showing the small grain of [Mo] K-OMS-2 with fringes ($d_{10\bar{3}\,\text{monoclinic}}$ = 0.304 nm) in parallel alignment on the margin of larger tetragonal grain with fringes ($d_{130\,\text{tetragonal}}$ = 0.310 nm).

DOI: 10.1021/acs.inorgchem.5b00906
Inorg. Chem. 2015, 54, 10163−10171

contact with, and overlain by, many irregular flakes. Lattice fringes and moiré patterns where grains are superimposed show that the small flakes are crystalline. Spacings of the diffraction or reciprocal lattice "rings" in the selected area electron diffraction (SAED) pattern correspond to those of K-OMS-2 and are indexed to the tetragonal unit cell (Figure 4b). However, fine structure of the "rings" with larger d^*, such as 121 and 031, shows that sets of spot pairs fall on reciprocal lattice rings with slightly different diameters, indicating that a structural distortion may occur. The higher magnification image in Figure 4c which corresponds to the area in the upper left in Figure 4a shows two grains in parallel alignment, both exhibiting lattice fringes. Fringes on the larger, bladed grain have measured spacings of 0.310 ± 0.004 nm, corresponding to the d_{130} planes in the tetragonal cell. Fringes on the smaller grains have a spacing of 0.304 ± 0.003 nm and are interpreted as corresponding to $d_{10\bar{3}}$ planes in the monoclinic cell based on the corresponding SAED results. **R-1:50** are highly suggestive that both tetragonal and monoclinic [Mo] K-OMS-2 are present as the bladed- and flake-shaped grains, respectively. Long dimensions of the monoclinic flakes appear to be bounded by planes that parallel the tunnel axis, where they can be indexed, e.g., (103), (101), with terminations such as (113).

To further verify the structural distortion due to Mo substitution, we studied the microstructures of **R-1:20** as this sample is fully comprised of ultrafine and crystalline flakes, similar to the small grains in **R-1:50** and **R-1:30**. The ultrafine particle sizes are advantageous to perform direct observations of the cross-section of 2 × 2 tunnels in the K-OMS-2 structure, which is particularly challenging for fiber-like morphologies with elongated tunnel lengths typical for regular K-OMS-2 reported in the literature. The HRTEM image of a single grain of **R-1:20** (Figure 5a) shows the orientation with the beam

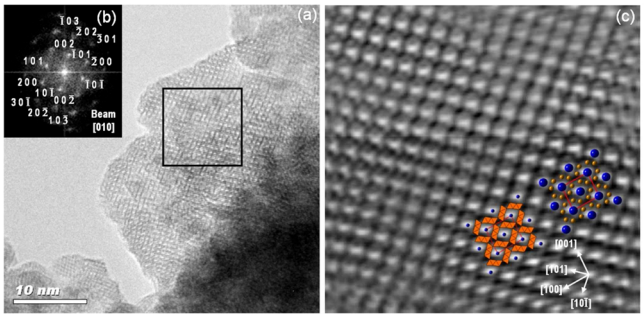

Figure 5. (a) Bright HRTEM image of [Mo] K-OMS-2 sample **R-1:20**. (b) Fourier transform pattern of the area enclosed by the black square in a, indexed using a monoclinic cell with [010] beam direction. (c) Fourier-filtered image of the area outlined in the black square in a. Structure drawings of monoclinic K-OMS-2 from Figure 1 are superimposed on this filtered image. Image filtering using Gatan Digital Micrograph.

direction parallel to the tunnel axis of [Mo] K-OMS-2. This grain orientation would correspond to a [001] zone axis image if the material had the tetragonal structure of K-OMS-2 (space group $I4/m$). Close inspection of the Fourier transform pattern (Figure 5b) and the Fourier-filtered image (Figure 5c) reveals that the expected 4-fold rotational symmetry of tetragonal structure was not present, further supporting structural distortion in the flake-like grains. We indexed the Fourier transform pattern (Figure 5b), alternatively, using a monoclinic cell with the beam direction along [010], corresponding to the tunnel axis in the monoclinic structure. Detailed measurements and the calculated d spacings of the four shortest translations with the monoclinic unit cell, the diagonals ([101] and [10$\bar{1}$]) and sides ([100] and [001]), are listed in Table 2 with the

Table 2. Calculation of Cell Parameters for Monoclinic R-1:20 from Measured Fringe Translations in the HRTEM Image (Figure 5), Calibrated by d Spacings from XRD (Table S-1)[a]

vector	measured (nm)	saled (Å)	plane	d_{hkl} (Å)
[100]	0.990 ± 0.004	10.35 ± 0.04	(100)	10.33
[001]	0.899 ± 0.003	9.40 ± 0.03	(001)	9.38
[101]	0.648 ± 0.006	6.78 ± 0.06	(101)	6.76
[101]	0.690 ± 0.004	7.22 ± 0.04	(101)	7.20

[a] $\beta = 93.747°$ obtained by applying the law of cosines to triangle with sides [100], [001], and 2 × [101]. Value confirmed by the measured angle between reciprocal lattice vectors 200 and 002 on the Fourier transform diffraction pattern, $\beta = 180 - \beta^* = 93.7 \pm 0.8°$. Scaled lengths of lattice vectors $[hkl]$ obtained from the length measured on the image by factor $d_{200}^{XRD}/[(d_{200}^{TEM} + d_{002}^{TEM})/2]$ with $d_{hkl}^{TEM} = [hkl]^{TEM} \sin \beta$.

measured $\beta = 93.747°$. The difference between d_{100} (10.33 Å) and d_{001} (9.38 Å) clearly confirms the transformation from the higher tetragonal symmetry to the lower symmetry monoclinic system. As shown by the aid of a schematic illustration superimposed on the Fourier-filtered image (Figure 5c), the square array of light spots corresponds to the pattern of low electron density associated with the 8-fold-coordinated potassium ions ($^{VIII}K^+$) occupying the tunnels, and the dark bands correspond to the high electron density of the manganese−oxygen octahedral framework. Since no special TEM sample preparation (e.g., ion-beam thinning, razor cutting, etc.) was involved, the HRTEM results showed the nature of the **R-1:20** crystals without artificial damage caused by sample preparation. We demonstrate the first direct evidence that shows structural distortions in cryptomelane-like MnO_2 due to single-species substitution. Natural minerals of manganese oxides commonly show structural distortions caused by diverse, multiple doping species with high doping contents.[29] Few artificial K-OMS-2 materials with single-species doping exhibit significant evolution in both shapes and phases with such a low substitution level as the [Mo] K-OMS-2 samples. Artificial multidopant K-OMS-2 (three different species) is a rare example in the literature which also apparently displays a morphology change, but knowing which species that results in the shape evolution is not possible.[24] Our results indicate single dopants with a high valency are enough to induce structural distortions. Before structural collapsing, the Mo-doped K-OMS-2 tends to release lattice stress by distorting the tetragonal cell to the monoclinic structure.

3.3. Spectroscopic Study. As structural distortion is strongly associated with the local environments of MnO_6 frameworks and dopants, we investigated their lattice vibration behavior by Raman and infrared spectroscopy. Raman peaks at 578 and 640 cm^{-1} are characteristic of K-OMS-2 (Figure 6).[14,30] The peak at 578 cm^{-1} is attributed to Mn−O vibrations along the lengths of the chains of edge-sharing MnO_6 octahedra, while that at 640 cm^{-1} is mainly due to Mn−O vibrations perpendicular to the MnO_6 octahedra double chains.[14,24] The presence of these two bands corresponds to the well-developed tetragonal structure of K-OMS-2. There is

DOI: 10.1021/acs.inorgchem.5b00906
Inorg. Chem. 2015, 54, 10163−10171

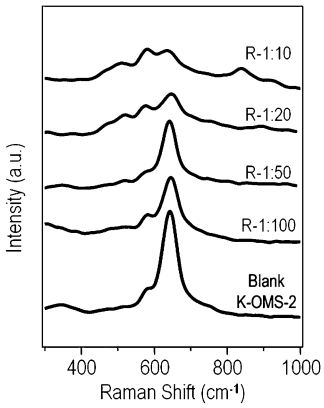

Figure 6. Raman spectra of **Blank K-OMS-2** (blank) and [Mo] K-OMS-2 materials.

no shift of the peak at 640 cm^{-1} with the increase of Mo content until **R-1:20** and **R-1:10**, showing the blue shift possibly due to the drastic decrease of their particle sizes.[31] In addition, the observed significant peak weakening at 640 cm^{-1} can be attributed to the altered distance of Mn−O bonds due to the monoclinic distortion.[32] This phenomenon was also observed in multidopant K-OMS-2, in which the non-fiber-like grains with fine sizes were shown.[24] The peak at 845 cm^{-1} in **R-1:10** is assigned to Mo−O−Mo vibrations,[33] attributed to the high Mo-substitution levels that lead to the formation of local molybdenum oxide clusters. The absence of Mo═O bonds in the regions of 310−370 and 890−1000 cm^{-1} indicates that no detectable segregation or particles of MoO_3 are present, showing the segregation-free substitution of Mo in the K-OMS-2 structures.[23] Concerning the insufficient sensitivity of XRD to identify the segregation issues of dopants, Raman spectroscopy can be a powerful tool to identify structural distortions in K-OMS-2.

The FT-IR spectra of the synthesized materials are shown in Figure 7. **Blank K-OMS-2** shows the well-defined absorption peaks at 469, 526, and 720 cm^{-1} as well as the poorly defined shoulder at 597 cm^{-1}, characteristic of K-OMS-2.[14,24,30,34] These are designated, from low wavenumber to high, as ν_5, ν_6, ν_7, and ν_8, according to the reported literature.[30] The peak at 720 cm^{-1} is specifically attributed to the stretching mode of MnO_6 octahedra along the chains. Incorporation of Mo in **R-1:100** shifts peaks ν_5 and ν_6 by +9 cm^{-1} relative to the corresponding peaks in **Blank K-OMS-2**, while the position of ν_8 was unchanged. The spectra for **R-1:50** and **R-1:20** appear strikingly different from the blank sample and from each other. Peaks in **R-1:20** are assigned as ν_6, ν_7, and ν_8. The blue shift of ν_5 and ν_6 in the doped K-OMS-2 may be caused by the changes of the reduced mass after Mo doping in the framework[24] and/or the lattice vacancies of metal cations in MO_6 octahedra. The peak ν_8 in **R-1:20** shifts to 703 cm^{-1} from 720 cm^{-1} in **Blank K-OMS-2**, and the peak ν_7 at 583 cm^{-1} was sharp and well resolved in contrast with the shoulder at 597 cm^{-1} in the blank sample. The red shift of MnO_6 lattice vibration can be due to longer Mn−O bond distances due to monoclinic distortion.[30] The peaks of **R-1:10** are similar to but weaker than **R-1:20**, showing a good agreement with the amorphous feature of the XRD signal. The IR band at around 1000 cm^{-1}, characteristic of Mo═O bonds, is not observed,[33] confirming again the homogeneous substitution of Mo in MnO_6 framework without segregation.

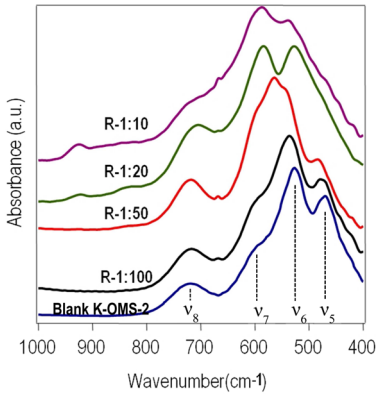

Figure 7. FT-IR spectra of **Blank K-OMS-2** (blank) and [Mo] K-OMS-2 materials. The four characteristic bands of pristine K-OMS-2 are ν_5 at 469 cm^{-1}, ν_6 at 526 cm^{-1}, ν_7 (shoulder) at 597 cm^{-1}, and ν_8 at 720 cm^{-1}.

3.4. Surface Area and Thermal Stability. We measured the surface areas (Table 1) and thermal stabilities of the synthesized materials. The surface areas of **Blank K-OMS-2**, **R-1:100**, and **R-1:50** are comparable to values reported for K-OMS-2 materials synthesized using similar methods.[20,35] **R-1:20** shows the largest surface area (213 m^2/g) among all the crystalline materials, which is 2.5 times higher than the pristine K-OMS-2. The high surface area may be attributed to the ultrafine nanoflakes observed in the TEM results. **R-1:10** has the highest surface area (347 m^2/g), which may arise from its amorphous feature.

The thermal stability of Mo-doped K-OMS-2 was evaluated by thermogravimetric analysis (TGA) profiles (Figure 8). The

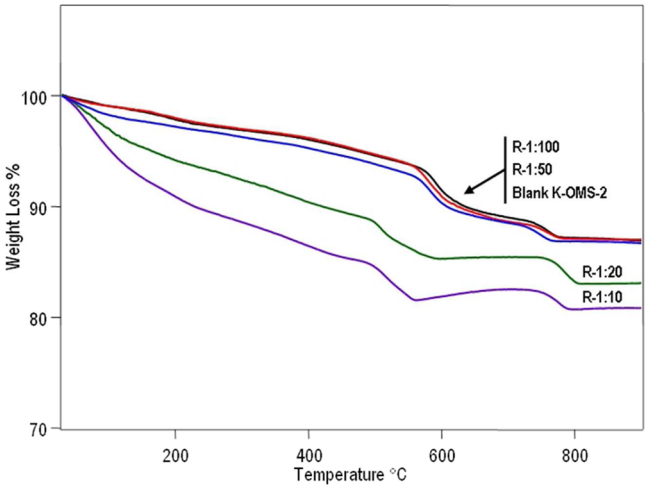

Figure 8. TGA profiles of the **Blank K-OMS-2** and the as-synthesized [Mo] K-OMS-2 materials.

thermal stabilities of these materials show three major weight losses in a range of 25−900 °C. The thermal stabilities of **Blank K-OMS-2** and low substituted samples (**R-1:100** and **R-1:50**) are similar and consistent with previous studies.[36] The weight loss between 25 and 250 °C is due to desorption of physisorbed H_2O and gaseous molecules from the surface. This is followed by desorption of chemically adsorbed H_2O up to 570 °C. The second major weight loss between 570 and 600 °C is caused by evolution of structural oxygen, which makes the K-OMS-2 structure unstable. The third major weight loss between 700

DOI: 10.1021/acs.inorgchem.5b00906
Inorg. Chem. 2015, 54, 10163−10171

and 750 °C is caused by the loss of framework oxygen, resulting in the phase transformation to Mn_3O_4. The highly substituted samples (**R-1:20** and **R-1:10**) show a similar three-step profile with higher weight losses. The first major weight losses of **R-1:20** and **R-1:10** are significantly higher than other samples, indicating a larger accumulation of water and other small molecules on their surfaces, consistent with their extremely large surface areas and ultrafine particle sizes. The temperature of their second weight loss is lower (~500 °C) as compared to 570 °C of the **Blank K-OMS-2**, showing a decrease in the thermal stability. This phenomenon may be associated with the weakened, prolonged Mn−O bonding due to distortions observed in the spectroscopic results.

3.5. Catalytic Test. We attempted to study the effect of structural distortions on the catalytic activity of K-OMS-2. To limit the catalytic contribution that comes from the dopant, we selected CO oxidation as the test reaction since molybdenum oxides are inactive for this catalytic reaction. In addition, we create a harsh condition for CO oxidation, such as high space velocity (35 000 $mL{\cdot}h^{-1}{\cdot}g_{cat}^{-1}$) and low oxygen concentration (only 2% O_2 in feed gas),[37] to give sufficient time for experimental operation, data recording, and effective comparisons of performance. As shown in Figure 9, the fibrous-shaped

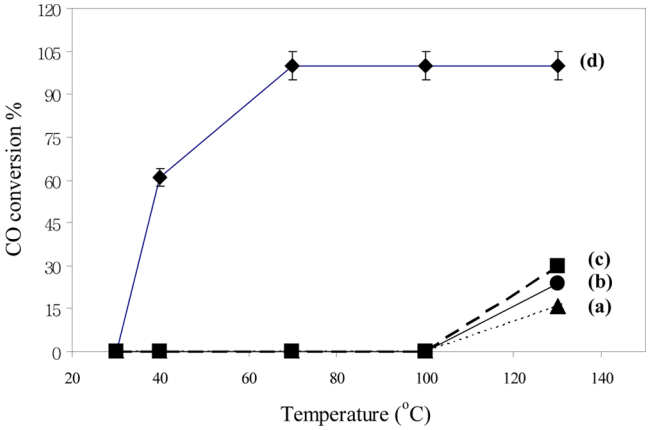

Figure 9. Catalytic performance of [Mo] K-OMS-2 materials for CO oxidation: (a) **R-1:50**, (b) **R-1:10**, (c) **Blank K-OMS-2**, and (d) **R-1:20**. Similar test using commercial MoO_3 samples showed no conversion under the same experimental conditions up to 150 °C.

materials of **Blank K-OMS-2** and **R-1:50** show similar activities as there is no onset catalytic conversion below 100 °C. The slightly higher conversion of **Blank K-OMS-2** (29%) over **R-1:50** (18%) at 130 °C might be due to the larger surface area of **Blank K-OMS-2** (Table 1). The ultrafine **R-1:20** exhibits significant catalytic activity at the much lowered onset temperature of 40 °C with a CO conversion of 61% and a complete conversion at 70 °C. The greatly lowered onset temperatures of **R-1:20** may suggest the presence of additional and/or new catalytic sites. **R-1:10** possesses the greatest surface area but displays low activity comparable to **Blank K-OMS-2** and **R-1:50**, indicating that the presence of a distorted K-OMS-2 structure is critical for efficient CO oxidation. Commercial MoO_3 powder was also tested under similar experimental conditions for comparison and found to be completely inactive up to 150 °C, confirming that the Mo^{6+} species is inert for CO oxidation. We further mixed the MoO_3 powder and **Blank K-OMS-2** with the same mole ratios of Mo/Mn in **R-1:20** for testing (Figure S-2). The results show weak CO oxidation activity similar to **Blank K-OMS-2**, suggesting that incorporation of Mo^{6+} and the relevant structural changes in K-OMS-2 (e.g., **R-1:20**) are critical to achieve the improved catalytic performance for CO oxidation.

4. DISCUSSION

4.1. Substitution Nechanism. To understand the potential substitution and structural-distortion mechanism, we followed the charge compensation scheme reported for tungsten- and multiple species-doped K-OMS-2,[21,24] based on the detailed elemental analysis summarized in Table 3. We used

Table 3. Elemental Analysis and the Experimentally Measured Average Oxidation State of [Mo] K-OMS-2 Materials

	K:Mn[a]		Mo:Mn[b]		
samples	AA	EDXS	XPS	EDXS	AOS_{meas}
Blank K-OMS-2	1:7.8	*c*	*c*	*c*	3.83
R-1:100	1:6.7	1:10	1:106	1:125	3.88
R-1:50	1:6.3	1:9.9	1:27	1:31	3.90
R-1:20	1:8.3	1:15	1:13.8	1:13.5	3.91
R-1:10	1:9.8	1:17	1:8.2	1:7.9	3.66

[a]Mole percents of K and Mn were determined by AA, while the ratios of Mo/Mn were determined by XPS due to the signal interferes between Mn and Mo in AA. [b]Semiquantitative elemental analyses of EDXS to confirm that the AA and XPS analyses are representative of individual grains. [c]Not applicable.

X-ray photoelectron spectroscopy (XPS) to identify the oxidation state of Mo in the doped samples first, as the redox approach in our synthesis may affect the oxidation state of Mo^{6+} in the final products. The binding energies of the Mo $3d_{3/2}$ and $3d_{5/2}$ transitions with an energy separation of 3.1 eV correspond well to the Mo^{6+} state in a MnOx environment (Figure S-3).[37,38] Following the charge imbalance in the octahedral framework with the presence of $^{VI}Mn^{3+}$ (the superscript of VI stands for VI-fold coordination) compensated by $^{VIII}K^{+}$ sitting in the tunnel sites, the resulting structural formula is shown as follows

$$K_x{Mn^{4+}}_{1-x}{Mn^{3+}}_xO_2 \quad (1)$$

in which observed values of x lie in the range 0.0625−0.1667 and the sum of molar $n_{Mn^{4+}} + n_{Mn^{3+}} = 1.0$ per 2.0 oxygen based on α-MnO_2 formula. Because of the presence of both Mn^{4+} and Mn^{3+} in K-OMS-2, we utilize values of the average oxidation state (AOS) of Mn to compare the contents of Mn^{3+} among the samples, which is expressed as follows

$$AOS = \frac{(4n_{Mn^{4+}} + 3n_{Mn^{3+}})}{(n_{Mn^{4+}} + n_{Mn^{3+}})} \quad (2)$$

where $n_{Mn^{4+}}$ and $n_{Mn^{3+}}$ are the number of moles of Mn^{4+} and Mn^{3+}, respectively.

Values of AOS of **Blank K-OMS-2** and Mo-doped samples measured by potentiometric titration (AOS_{meas}) are listed in Table 3, while those calculated (AOS_{calcd}) from elemental analyses are listed with structural formulas in Table 4. The value of AOS_{calcd} = 3.87 for **Blank K-OMS-2** closely matches the experimental one (AOS_{meas} = 3.83), validating that mixed valency can be accounted by the structural formula in eq 1.

We consider [Mo] K-OMS-2 as a substitutional solid solution in which $^{VI}Mo^{6+}$ potentially (radius of 0.73 Å)

DOI: 10.1021/acs.inorgchem.5b00906
Inorg. Chem. 2015, 54, 10163−10171

Table 4. Structural Formula of [Mo] K-OMS-2 Calculated from AA and XPS Analyses

sample	K/ $Mn_{(AA)}$	Mo/ $Mn_{(XPS)}$	structural formula[a]	AOS_{calcd}[b]
Blank K-OMS-2	0.128		$K_{0.128}Mn^{4+}_{0.872}Mn^{3+}_{0.128}O_2$	3.872
R-1:100	0.149	0.009	$K_{0.146}Mo_{0.009}\square^{\circ}_{0.009}Mn^{4+}_{0.854}Mn^{3+}_{0.128}O_2$	3.870
R-1:50	0.159	0.037	$K_{0.148}Mo_{0.034}\square^{\circ}_{0.034}Mn^{4+}_{0.852}Mn^{3+}_{0.079}O_2$	3.915
R-1:20	0.120	0.072	$K_{0.105}Mo_{0.063}\square^{\circ}_{0.063}Mn^{4+}_{0.873}Mn^{3+}_{0.000}O_2$	4.000
R-1:10	0.102	0.122	*c*	*c*

[a]Moles cation calculated from mole ratio K/Mn and Mo/Mn by setting $n_{Mn} + 2n_{Mo} = 1.0$. [b]Allocation of total manganese between Mn^{4+} and Mn^{3+} and calculation of average oxidation state are derived from charge balance based on setting moles oxygen =2.0. [c]Not applicable.

substitutes for both $^{VI}Mn^{3+}$ and $^{VI}Mn^{4+}$ (radii of 0.67 and 0.79 Å, respectively) in the octahedral framework due to their similar crystal radii.[38,39] Both exchange mechanisms involve creation of cation vacancies in the octahedral framework to balance charge.[21] Substitution of $^{VI}Mo^{6+}$ for $^{VI}Mn^{3+}$ in the octahedral framework is described by the following exchange

$$^{VI}MO^{6+} + ^{VI}\square^{\circ} \leftrightarrow 2^{VI}Mn^{3+} \quad (3)$$

where $^{VI}\square^{\circ}$ is an octahedral vacancy in the framework required to balance charge. The resulting structural formula following eq 1 is

$$K_xMo^{6+}{}_y\square^{\circ}{}_yMn^{4+}{}_{1-x}Mn^{3+}{}_{x-2y}O_2 \quad (4)$$

The value of $n_{Mo} = 0.063$ in **R-1:20** is close to the maximum allowed by the structural formula of eq 4, where $n_K = 0.128$. According to the mole proportions of K, Mn, and Mo (see Supporting Information), the generation of crystalline product (cryptomelane-like structure) in sample **R-1:10** cannot be achieved where the concentration of Mo in the synthesis mixture exceeded $(1/2)n_K$ in **Blank K-OMS-2**. This critical correlation between $n_{Mo^{6+}}$ and $n_{Mn^{3+}}$ supports our assumption that Mo^{6+} substitutes for Mn^{3+} in [Mo] K-OMS-2. In addition, the values of AOS_{calcd} are directly proportional to n_{Mo} and reach the maximum, AOS = 4.0, where $n_{Mo} = (1/2)n_K$. This trend fits that of the experimentally measured AOS_{meas} very well. The values of AOS_{calcd} in Table 4 closely approximate values of AOS_{meas}, with differences no greater than 2.3%. There is no structural control of charge balance in **R-1:10**, and AOS_{meas} = 3.66 is substantially lower than the minimum allowed in the K-OMS-2 structure.

We also considered the possibility that $^{VI}Mo^{6+}$ substitutes for $^{VI}Mn^{4+}$. The exchange analogous to eq 3 above is

$$2^{VI}Mo^{6+} + ^{VI}\square^{\circ} \leftrightarrow 3^{VI}Mn^{4+} \quad (5)$$

which leads to the formula

$$K_xMo^{6+}{}_{2y}\square^{\circ}{}_yMn^{4+}{}_{1-x-3y}Mn^{3+}{}_xO_2 \quad (6)$$

The maximum value for $n_{Mo} = 2n_K = 0.33$, where the tunnel site is 2/3 occupied. The high concentration of octahedral vacancies would lead to structural collapse before the limit is reached. The formula following eq 6 requires AOS to decrease as n_{Mo} increases, opposite to the experimental observation of AOS_{meas}. These results reveal that Mo substitutes for Mn^{3+} as the major pathway, which rationalizes the substitution limit observed in K-OMS-2.

4.2. Structural and Morphological Evolution. Diverse doping and substitutions in K-OMS-2 materials have been conducted, but no clear evidence of morphological evolution associated with structural distortion was demonstrated. A recent study of multispecies substitution in K-OMS-2 shows the flake assembly of spheres, but the complicated doping system leads to a difficulty in understanding the clear correlation between the dopant species and morphology changes.[24] On the other hand, the previous work of single species-doped K-OMS-2 with hexavalent tungsten, however, demonstrates XRD peak broadening but no shape changes, possibly due to the insufficient doping amount of tungsten (less than 4%).[21] As mentioned above, shape change with relatively low-valent species (In^{3+}, Co^{3+}, Cu^{2+}, etc.) has been barely reported.[22,27] These observations, together with our results, may be rationally explained by the proposed substitution mechanism. The low-valent dopants that exchange with Mn^{3+} in K-OMS-2 do not involve generation of cation vacancies, and thus, morphology changes of the doped products are rare. For high-valent species (e.g., Mo^{6+}, W^{6+}, etc.), each exchange with Mn^{3+} would generate one vacancy, easily resulting in an unstable framework, as well as the shape changing and distorted structure, even with relatively low doping amounts.

The structural-distortion route from tetragonal to monoclinic to structural collapse was identified for the first time in K-OMS-2. Apparently, **R-1:20** is the "structural tolerance limit" of Mo substitution following this route to stabilize the structure. The tetragonal OMS-2 crystal always has a highly 1-D morphology preferred for many different synthetic methods and conditions, indicating that tetragonal K-OMS-2 grows rapidly along the tunnel axis direction of [001]. Molybdenum can dissolve in the tetragonal structure up to a limit somewhat in excess of that observed in **R-1:100**. Synthesis of mixtures with higher concentrations of Mo leads to nucleation and growth of monoclinic nanoflakes. This may result in a two-phase mixture of Mo-poor tetragonal 1D crystals and Mo-rich monoclinic nanoflakes. The nucleation and growth of monoclinic flakes are suggested to inhibit rates of growth of tetragonal 1D crystals along their length, leading to a decrease in aspect ratio with increasing Mo concentrations in the synthesis mixture. The equidimensional nanoflakes in **R-1:20** without the presence of any other forms of morphologies may suggest a homogeneous distribution of Mo species. **R-1:50** are plausibly identified as the transition stage of this morphological evolution process. **R-1:30** with a doping level between **R-1:50** and **R-1:20** shows mixed morphologies of cube-like particles (the even smaller aspect ratios than the blade particles in **R-1:50**) and fine nanoflakes. These results demonstrate that **R-1:30** at the transition stage bridges **R-1:50** and **R-1:20.** Thus, the Mo doping in K-OMS-2 could be homogeneous with low Mo levels (before transition state of **R-1:100**) but plausibly inhomogeneous within the transition state (**R-1:50** to **R-1:30**). In addition, **R-1:20** approaches the substitution limit and preserves the crystalline structure with ultrafine sizes of crystals, implying maximized defects available for catalysis. Further Mo incorporation with even higher amounts of vacancies and crystal distortion energy results in the complete destruction of crystal phases in **R-1:10**.

4.3. Structural-Distortion Induced Catalytic Enhancement. The distorted monoclinic K-OMS-2 structure may directly result in the markedly enhanced catalytic activity. The proposed vacancies of Mn^{3+} in MnO_6 octahedra may yield

DOI: 10.1021/acs.inorgchem.5b00906
Inorg. Chem. 2015, 54, 10163−10171

weakly bonded lattice oxygen. In addition, both the relatively long Mn−O bonds (spectroscopic results in Figure 6 and 7) and weaker lattice oxygen stabilities (TGA data in Figure 8) suggest the presence of flexible lattice oxygen that can perform rapid exchange with molecular oxygen and carbon monoxide for efficient catalysis, particularly for the defect-maximized **R-1:20**.[40] The charge-compensation mechanism and AOS results show that the population of Mn^{3+} is greatly reduced after Mo substitution. As the catalytic activities of K-OMS-2 due to the mixed valence of Mn^{3+}/Mn^{4+} are well recognized,[13] the highly efficient catalysis of **R-1:20** (compared to **Blank K-OMS-2**) may not directly depend on the factor of mixed valency. The weakly bonded oxygen in the monoclinic K-OMS-2 due to structural distortions contributes greatly to the enhanced catalytic performance for CO oxidation.

The catalytic performance was demonstrated to be highly dependent on the presence of the K-OMS-2 structure (XRD in Figure 2), implying that the characteristic 2 × 2 tunnels of K-OMS-2 are potentially responsible for the additional catalytically active sites. **R-1:10** without the active sites constructed based on the lattice geometry of 2 × 2 tunnels thus suffers from the low catalytic activity. The molecular sizes of carbon monoxide and molecular oxygen are small enough to diffuse into the 2 × 2 tunnels.[41] The ultrafine flake morphology greatly shortens the length of tunnels, making the interior space of the tunnels easily accessible for CO oxidation. In contrast, **Blank K-OMS-2** with 1D rod-like morphology (much longer length of tunnels) hinders the CO from reaching the interior active sites deep inside the tunnels. Thus, the highest catalytic activities of **R-1:20** of all K-OMS-2 samples studied here can be rationalized. The low contents of nanoflakes in **R-1:50**, indicated by the lowest surface area (even lower than **Blank K-OMS-2**), may not be sufficient enough to contribute appreciable catalytic enhancement as does **R-1:20**.

5. CONCLUSIONS

This work demonstrates the strong dependence of a distorted monoclinic structure of K-OMS-2 on the catalytic performance. **R-1:20** exhibits significantly improved catalytic activity for CO oxidation with the onset temperature as low as 40 °C compared to that of 130 °C for nonmodified K-OMS-2. Such drastic catalytic enhancement comes solely from structural distortions. Detailed characterization of the structural distortion provides an informative signature for identifying monoclinic K-OMS-2. The structural distortion and shape changes of [Mo] K-OMS-2 are highly associated with the presence of vacancies in the MnO_6 framework, which arises from substitution of Mo^{6+} for Mn^{3+} as the major pathway. These findings not only help interpret catalytic results comprehensively with doped K-OMS-2 as catalysts but also may establish a new design and controlled preparation for highly efficient catalysts of doped K-OMS-2.

■ ASSOCIATED CONTENT

Supporting Information

The Supporting Information is available free of charge on the ACS Publications website at DOI: 10.1021/acs.inorgchem.5b00906.

Detailed information on crystal parameters, calculation of mole proportions for substitution mechanism, TEM images of Mo-doped K-OMS-2 materials, catalytic data of MoO_3 and Blank K-OMS-2, and XPS measurement (PDF)

■ AUTHOR INFORMATION

Corresponding Author

*E-mail: steven.suib@uconn.edu.

Notes

The authors declare no competing financial interest.

■ ACKNOWLEDGMENTS

We acknowledge the support of the U.S. Department of Energy, Office of Basic Energy Sciences, Division of Chemical Sciences, Geosciences, and Biosciences for support of this research under contract DE-FG02-86ER13622. We thank Dr. Heng Zhang and Dr. Yang Hsiang Chan for XPS measurements and Dr. Francis Galasso, Dr. Craig Calvert, Lei Jin, and Cecil King'ondu Kithongo for helpful discussions and experiments.

■ REFERENCES

(1) Suib, S. L. *Acc. Chem. Res.* **2008**, *41*, 479−487.
(2) Feng, Q.; Kanoh, H.; Miyai, Y.; Ooi, K. *Chem. Mater.* **1995**, *7*, 148−153.
(3) Johnson, C. S.; Mansuetto, M. F.; Thackeray, M. M.; Shao-Horn, Y.; Hackney, S. A. *J. Electrochem. Soc.* **1997**, *144*, 2279−2283.
(4) Hettiarachchi, G. M.; Pierzynski, G. M.; Ransom, M. D. *Environ. Sci. Technol.* **2000**, *34*, 4614−4619.
(5) Chen, C. H.; Jin, L.; Espinal, A. E.; Firliet, B. T.; Xu, L. P.; Aindow, M.; Joesten, R.; Suib, S. L. *Small* **2010**, *6*, 988−992.
(6) Son, Y. C.; Makwana, V. D.; Howell, A. R.; Suib, S. L. *Angew. Chem., Int. Ed.* **2001**, *40*, 4280−4283.
(7) Jin, L.; Reutenauer, J.; Opembe, N.; Lai, M.; Martenak, D. J.; Han, S.; Suib, S. L. *ChemCatChem* **2009**, *1*, 441−444.
(8) Kijima, N.; Takahashi, Y.; Akimoto, J.; Awaka, J. *J. Solid State Chem.* **2005**, *178*, 2741−2750.
(9) Li, X.; Hu, B. X.; Suib, S.; Lei, Y.; Li, B. K. *J. Power Sources* **2010**, *195*, 2586−2591.
(10) Abecassis-Wolfovich, M.; Jothiramalingam, R.; Landau, M. V.; Herskowitz, M.; Viswanathan, B.; Varadarajan, T. K. *Appl. Catal., B* **2005**, *59*, 91−98.
(11) Gandhe, A. R.; Rebello, J. S.; Figueiredo, J. L.; Fernandes, J. B. *Appl. Catal., B* **2007**, *72*, 129−135.
(12) Chen, C.-H.; Suib, S. L. *J. Chin. Chem. Soc.* **2012**, *59*, 465−472.
(13) Hou, J.; Li, Y.; Mao, M.; Zhao, X.; Yue, Y. *Nanoscale* **2014**, *6*, 15048−15058.
(14) Gao, T.; Glerup, M.; Krumeich, F.; Nesper, R.; Fjellvag, H.; Norby, P. *J. Phys. Chem. C* **2008**, *112*, 13134−13140.
(15) Chen, J. L.; Tang, X. F.; Liu, J. L.; Zhan, E. S.; Li, J.; Huang, X. M.; Shen, W. J. *Chem. Mater.* **2007**, *19*, 4292−4299.
(16) Shen, X.; Morey, A. M.; Liu, J.; Ding, Y.; Cai, J.; Durand, J.; Wang, Q.; Wen, W.; Hines, W. A.; Hanson, J. C.; Bai, J.; Frenkel, A. I.; Reiff, W.; Aindow, M.; Suib, S. L. *J. Phys. Chem. C* **2011**, *115*, 21610−21619.
(17) Hu, B. X.; Chen, C. H.; Frueh, S. J.; Jin, L.; Joesten, R.; Suib, S. L. *J. Phys. Chem. C* **2010**, *114*, 9835−3844.
(18) Chen, J. L.; Li, J.; Li, H. J.; Huang, X. M.; Shen, W. J. *Microporous Mesoporous Mater.* **2008**, *116*, 586−592.
(19) Cai, J.; Liu, J.; Willis, W. S.; Suib, S. L. *Chem. Mater.* **2001**, *13*, 2413−2422.
(20) Chen, X.; Shen, Y.-F.; Suib, S. L.; O'Young, C. L. *Chem. Mater.* **2002**, *14*, 940−948.
(21) Calvert, C.; Joesten, R.; Ngala, K.; Villegas, J.; Morey, A.; Shen, X.; Suib, S. L. *Chem. Mater.* **2008**, *20*, 6382−6388.
(22) Liu, Z.; Xing, Y.; Chen, C.-H.; Zhao, L.; Suib, S. L. *Chem. Mater.* **2008**, *20*, 2069−2071.
(23) Polverejan, M.; Villegas, J. C.; Suib, S. L. *J. Am. Chem. Soc.* **2004**, *126*, 7774−7775.
(24) King'ondu, C. K.; Opembe, N.; Chen, C.-H.; Ngala, K.; Huang, H.; Iyer, A.; Garcés, H. F.; Suib, S. L. *Adv. Funct. Mater.* **2011**, *21*, 312−323.

DOI: 10.1021/acs.inorgchem.5b00906
Inorg. Chem. 2015, 54, 10163−10171

(25) Lan, W.-J.; Kuo, C.-C.; Chen, C.-H. *Chem. Commun.* **2013**, *49*, 3025−3027.
(26) Xia, G.-G.; Tong, W.; Tolentino, E. N.; Duan, N.-G.; Brock, S. L.; Wang, J.-Y.; Suib, S. L.; Ressler, T. *Chem. Mater.* **2001**, *13*, 1585−1592.
(27) Hu, B.; Chen, C.-H.; Frueh, S. J.; Jin, L.; Joesten, R.; Suib, S. L. *J. Phys. Chem. C* **2010**, *114*, 9835−9844.
(28) Sasaki, T.; Komaba, S.; Kumagai, N.; Nakai, I. *Electrochem. Solid-State Lett.* **2005**, *8*, A471−A475.
(29) Turner, S.; Buseck, P. R. *Science* **1981**, *212*, 1024−1027.
(30) Julien, C. M.; Massot, M.; Poinsignon, C. *Spectrochim. Acta, Part A* **2004**, *60A*, 689−700.
(31) Zhang, F.; Chan, S.-W.; Spanier, J. E.; Apak, E.; Jin, Q.; Robinson, R. D.; Herman, I. P. *Appl. Phys. Lett.* **2002**, *80*, 127−129.
(32) Kartopu, G.; Lahmar, A.; Es-Souni, M. *Appl. Phys. Lett.* **2008**, *92*, 151910−151910.
(33) Seguin, L.; Figlarz, M.; Cavagnat, R.; Lassegues, J. C. *Spectrochim. Acta, Part A* **1995**, *51A*, 1323−1344.
(34) Nyutu, E. K.; Chen, C.-H.; Dutta, P. K.; Suib, S. L. *J. Phys. Chem. C* **2008**, *112*, 9659−9667.
(35) Sithambaram, S.; Xu, L.; Chen, C.-H.; Ding, Y.; Kumar, R.; Calvert, C.; Suib, S. L. *Catal. Today* **2009**, *140*, 162−168.
(36) Ding, Y.-S.; Shen, X.-F.; Sithambaram, S.; Gomez, S.; Kumar, R.; Crisostomo, V. M. B.; Suib, S. L.; Aindow, M. *Chem. Mater.* **2005**, *17*, 5382−5389.
(37) Chen, C. H.; Njagi, E. C.; Sun, S. P.; Genuino, H.; Hu, B. X.; Suib, S. L. *Chem. Mater.* **2010**, *22*, 3313−3315.
(38) Shannon, R. D. *Acta Crystallogr., Sect. A: Cryst. Phys., Diffr., Theor. Gen. Crystallogr.* **1976**, *A32*, 751−767.
(39) Shannon, R. D.; Prewitt, C. T. *Acta Crystallogr., Sect. B: Struct. Crystallogr. Cryst. Chem.* **1969**, *25*, 925−946.
(40) Njagi, E. C.; Chen, C. H.; Genuino, H.; Galindo, H.; Huang, H.; Suib, S. L. *Appl. Catal., B* **2010**, *99*, 103−110.
(41) Luo, J.; Zhang, Q.; Garcia-Martinez, J.; Suib, S. L. *J. Am. Chem. Soc.* **2008**, *130*, 3198−3208.

DOI: 10.1021/acs.inorgchem.5b00906
Inorg. Chem. 2015, 54, 10163−10171